AGU PUBLICATIONS

JGR

Journal of Geophysical Research: Planets

RESEARCH ARTICLE
10.1002/2013JE004524

Key Points:

- Faulting along Eastern Olympus Mons Basal Scarp resembles a landslide
- Numerical models suggest failure occurs if water and a detachment exist at depth
- Models indicate water existed at depth, influencing volcanic evolution

Supporting Information:

- Readme
- Figure S1a
- Figure S1b
- Figure S2a
- Figure S2b
- Figure S3a
- Figure S3b
- Figure S4a
- Figure S4b
- Figure S5a
- Figure S5b
- Text S1
- Table S1

Correspondence to:
M. B. Weller,
matt.b.weller@rice.edu

Citation:
Weller, M. B., P. J. McGovern, T. Fournier, and J. K. Morgan (2014), Eastern Olympus Mons Basal Scarp: Structural and mechanical evidence for large-scale slope instability, *J. Geophys. Res. Planets*, *119*, doi:10.1002/2013JE004524.

Received 6 SEP 2013
Accepted 27 MAR 2014
Accepted article online 7 APR 2014

Eastern Olympus Mons Basal Scarp: Structural and mechanical evidence for large-scale slope instability

M. B. Weller[1], P. J. McGovern[2], T. Fournier[1,3], and J. K. Morgan[1]

[1]Department of Earth Science, Rice University, Houston, Texas, USA, [2]Lunar and Planetary Institute, Houston, Texas, USA, [3]Shell International Exploration and Production, Houston, Texas, USA

Abstract The expression of the Eastern Olympus Mons Basal Scarp (EOMBS) is seemingly unique along the edifice. It exhibits two slope-parallel structures: a nearly 100 km long upslope extensional normal fault system and a downslope contractional wrinkle ridge network, a combination that is found nowhere else on Olympus Mons. Through structural mapping and numerical modeling of slope stability of the EOMBS, we show that these structures are consistent with landsliding processes and volcanic spreading. The EOMBS is conditionally stable when the edifice contains pore fluid, and critically stable, or in failure, when the edifice contains a dipping overpressured confined aquifer and mechanical sublayer at depth. Failure of the fault-bounded portion of the flank results in estimated volumes of material ranging from 5600–6900 km^3, or 32–39% of the estimated volume of the "East" Olympus Mons aureole lobe. We suggest that the EOMBS faults may be an expression of early stage flank collapse and aureole lobe formation. Ages of deformed volcano adjacent plains associated with the wrinkle ridges indicate that this portion of the edifice may have been tectonically active at $<$ 50 Ma and may be coeval with estimated ages of adjacent outflow channels, 25–40 Ma. This observation suggests that conditions that favor flank failure, such as water at depth below the edifice, existed in the relatively recent past and potentially could drive deformation to the present day.

1. Introduction

The Olympus Mons edifice, extending to an elevation of 23 km above its base, towers above all other volcanoes in the Solar System. The nearly 600 km diameter edifice is located in the northwest of the Tharsis Rise on Mars (Figure 1a) and is partially bounded by an escarpment of up to 10 km height, known as the Olympus Mons basal scarp (Figure 1b). Adjacent to the basal scarp are deposits that exhibit rugged lobate morphologies, known as the Olympus Mons aureole lobes (Figure 1b). The aureole lobes discontinuously extend hundreds of kilometers from the edifice. Both the expressions of the aureole lobes and the structure of the Olympus Mons edifice exhibit strong asymmetries, with the greatest extent and elongation to the northwest and the least extent and shorter dimension to the southeast, respectively. The proximity of the basal scarp to the aureole lobes suggests a causal relationship between these features [*Harris*, 1977; *Lopes et al.*, 1980, 1982; *Francis and Wadge*, 1983; *Tanaka*, 1985; *McGovern and Solomon*, 1993; *Mouginis-Mark*, 1993; *McGovern et al.*, 2004a; *De Blasio*, 2011]. Limited resolution data sets in the past, however, have made it difficult to conclusively demonstrate such a link.

The origin of the aureole lobes that surround Olympus Mons is still debated. However, the work of *McGovern et al.* [2004a], using topography data from the Mars Orbiter Laser Altimeter (MOLA) greatly improved the characterizations of these structures along the northwestern flank. Furthermore, *McGovern et al.* [2004a] demonstrated that at least two of the aureole lobes, oriented to the north and northwest, originated from the volcano's flanks in large, likely catastrophic, landslide events that left headwalls along the periphery of the edifice that now constitute the basal scarp. To date, however, no direct observation of such edifice collapse has been made, and edifice failure remains only one of several hypotheses that attempt to explain the formation of the aureole deposits. In order to test and validate the flank collapse hypothesis, we use constraints obtained through structural mapping and analysis, to develop plausible subsurface configurations for use in slope stability analysis of the Eastern Olympus Mons Eastern Basal Scarp (EOMBS).

1.1. Aureole Lobe and Basal Scarp Formation Mechanisms

Hypotheses for the formation of the Olympus Mons aureole lobes and basal scarp naturally fall into two categories: volcanic products and flank failure. The first category of formation mechanisms suggests that the

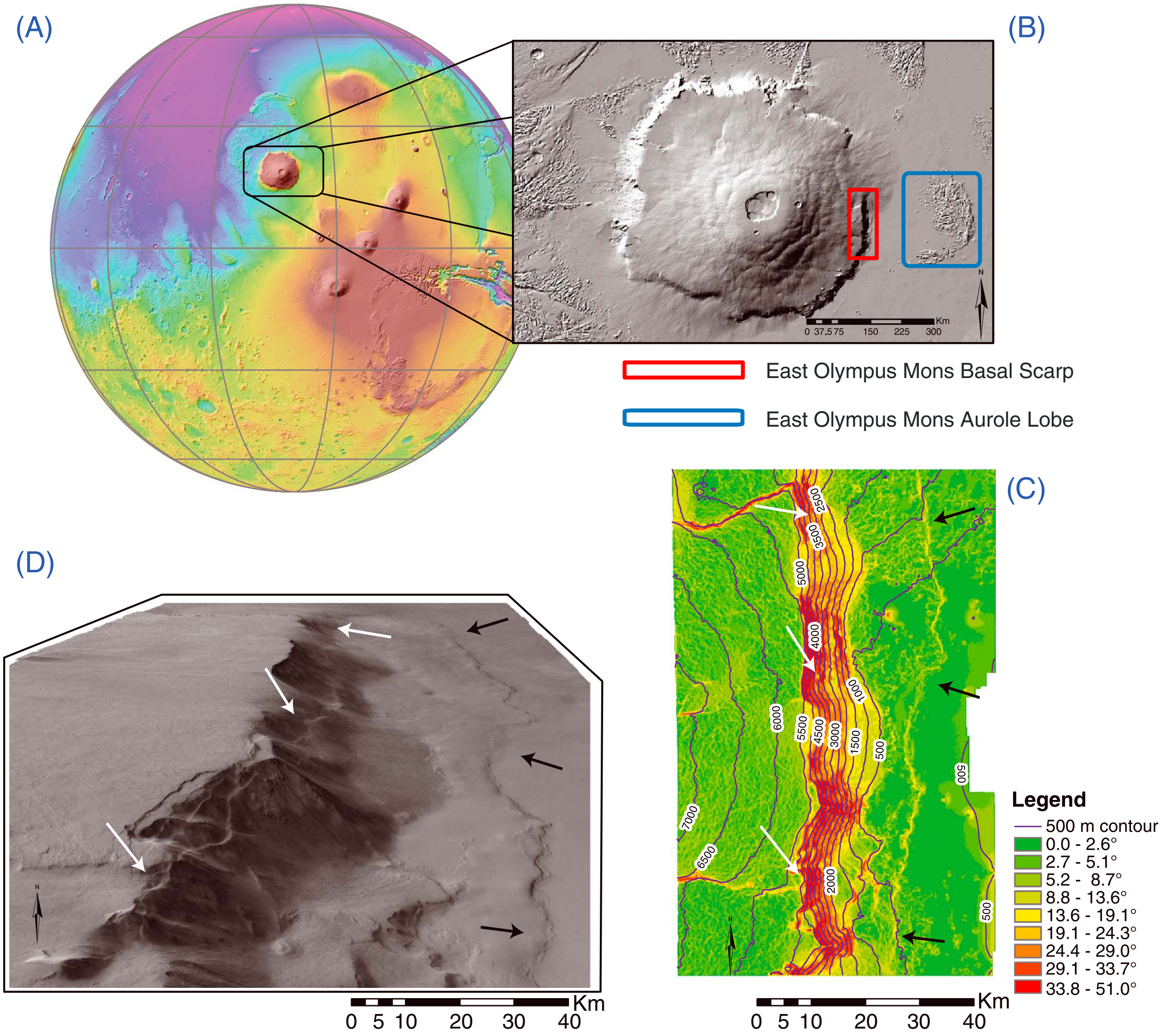

Figure 1. (a) Western Hemisphere orthographic projection of MOLA elevation data [*Smith et al.*, 2001]. (b) THEMIS [*Christensen et al.*, 2004] daytime IR mosaic of the Olympus Mons region. The study area is highlighted by the red box. Eastern Olympus Mons aureole lobe is indicated by the blue box. (c) 500 m contoured and slope map planar view of the Eastern Olympus Mons Basal Scarp (EOMBS, red box) from HRSC-derived DTM. (d) HRSC [*Gwinner et al.*, 2007] 3-D DTM (created as a HRSC image over a HRSC-derived DTM) of the Eastern Olympus Mons Basal Scarp (EOMBS, red box). White arrows indicate extensional fault traces, and black arrows indicate contractional fault (wrinkle ridges) traces.

aureoles are the products of volcanism, such as pyroclastic or effusive volcanic flows [*Morris*, 1982; *Carr*, 1973; *Morris and Tanaka*, 1994] that were emplaced locally, i.e., from a source region immediately below the deposits themselves that may have predated the emplacement of the Olympus Mons edifice. In these models, the basal scarp of Olympus Mons has no direct relationship to the aureole lobes. The directions of flow that can be inferred from the distributions of ridges within the lobe, and boundary features, allow for the identification of potential source vents within the aureoles [*Morris*, 1982]. Analysis of Viking imagery indicated an apparent absence of bedding within the aureoles. This led to the interpretation that the aureole lobes were “thick, easily eroded deposits typical of unwelded ash” [*Morris*, 1982]. *Wilson and Mouginis-Mark* [2003] further asserted that the ridges near the edge of the northernmost aureole lobe had originated via explosive eruptions initiated by an intrusion.

The second proposed formation mechanism is flank failure. Within this view, the aureoles have been inferred to be material that is directly derived from the slopes of the Olympus Mons edifice as either mass-wasting events, perhaps catastrophic in nature [*Lopes et al.*, 1980, 1982], or as gravity spreading of local sediments or flank material at low strain rates [*Francis and Wadge*, 1983; *Tanaka*, 1985]. *Tanaka* [1985] proposed that ice served as a basal lubricant for gravity sliding. Other models of edifice failure invoked the presence of liquid water via reconstructed paleoshorelines for a northern global ocean, suggesting that the basal scarp may have been cut by wave action [e.g., *Mouginis-Mark*, 1993; *De Blasio*, 2011]. *Lopes et al*. [1980, 1982] proposed that the large submarine landslides off the Hawaiian seamount chain detected by *Moore* [1964] are the closest Earth analogs in scale and morphology to the Olympus Mons aureoles. Subsequent mapping of the submarine landslides and slumps along the flanks of Hawaiian volcanoes [*Moore et al*., 1989], and mapping derived from the Mars Orbiter Camera by *McGovern et al*. [2004a], showing layering within the northern aureole blocks, strengthens the suggestion of *Lopes et al*. [1980, 1982] that both the Kilauea landslides and the Olympus Mons aureole lobes are analogous features of volcano-derived landslides. In addition, geodetic, seismicity, and reflection seismic studies strongly indicate the presence of horizontal/subhorizontal basal detachment faults (décollements) at the bases of the Hawaiian volcanic edifices, which in turn have provided a means for the outward spreading of Hawaiian volcanic flanks [e.g., *Owen et al*., 1995, 2000; *Denlinger and Okubo*, 1995; *Morgan et al*., 2000]. *McGovern and Solomon* [1993] modeled stresses within edifices with basal detachments, and their results support the suggestion that the Hawaiian landslides and the aureoles, linked to the high-angle Pali faults on Kilauea and to the Olympus Mons basal scarp, respectively, are analogous features. *McGovern and Morgan* [2009] further inferred that the geometry of the current Olympus Mons edifice, with a prominent northwest-southeast asymmetry, is consistent with that of a spreading volcano underlain by a basal décollement and that the primary spreading axis is oriented the northwest-southeast, with northwest oriented spreading most prominent (coincident with the largest expanse of aureole deposits). Further, results of analogue modeling of gravity-driven deformation of Olympus Mons are also consistent with the volcano being detached from its basement [*Byrne et al*., 2013].

1.2. New Evidence for Flank Failure

Although improved imagery demonstrates a link between the aureole lobes and edifice material, suggesting a catastrophic sector collapse [*McGovern et al*., 2004a], structural evidence of an aureole-forming event within the scarp has not been discovered, and of course, no such event has ever been directly observed on Mars. Broadly, evidence linking the edifice to an aureole lobe from an aureole-forming event would need to meet the following criteria: A clearly defined and continuous head scarp; linked along slope failure planes (faults) with clear indications of extension within the slope, and contraction along the toe; indications of large-scale instability along slope; and a clearly identified radially deposited aureole lobe. Here we show that these criteria are met, and structural evidence exists along the eastern basal scarp. Two approximately parallel structures along the nearly 7 km high eastern basal scarp are identified as probable faults (white and black arrows; Figures 1c and 1d). *Borgia et al*. [1990] were the first to identify some of these structures along the EOMBS. They identified a wrinkle ridge compressional fault system within the plains immediately adjacent to the basal scarp; however, given the coarse resolution of the Viking orbiter data (150–300 m/pixel), they were unable to unambiguously identify the corresponding fault system along the slope of the scarp face, suggesting that it could be normal faulting. In contrast, *Basilevsky et al*. [2006] identified both structures, the on-scarp fault and downslope plains faults, as wrinkle ridges. Additionally, *Basilevsky et al*. [2006] dated the age of the faulted plains adjacent to the basal scarp through crater counting statistics, arguing that it is a young surface of less than 50 Ma (≤ 30–50 Ma in the study region, and < 25–40 Ma southeast of the EOMBS). This would imply that the deformation recorded here is one of the youngest recognized events on the planet and that it might even reflect ongoing processes.

The recent release of data products from the High Resolution Stereo Camera (HRSC) aboard the Mars Express orbiter, with maximum and nominal resolutions of 2 m and 10 m, respectively, has made digital terrain models (DTMs) with improved resolutions of up to 50 m possible [*Gwinner et al*., 2007]. Using these data products, we have reexamined the upslope and downslope fault systems discussed above. We interpret these faults in the context of a slope failure model and determine the stability of the edifice using limit equilibrium techniques constrained by surface observations.

In order to test the validity of these fault systems being linked and bounding a large incipient landslide, we carried out structural mapping (section 2) of the EOMBS to help identify and constrain subedifice structures and geometries. We then ran numerical slope stability calculations on five transects (R1–R5; Figure 2), for a wide range of possible subedifice structures, geometries, and mechanical properties, to determine which configuration generates the greatest chance of failure (section 3). From these analyses, we show that faulting

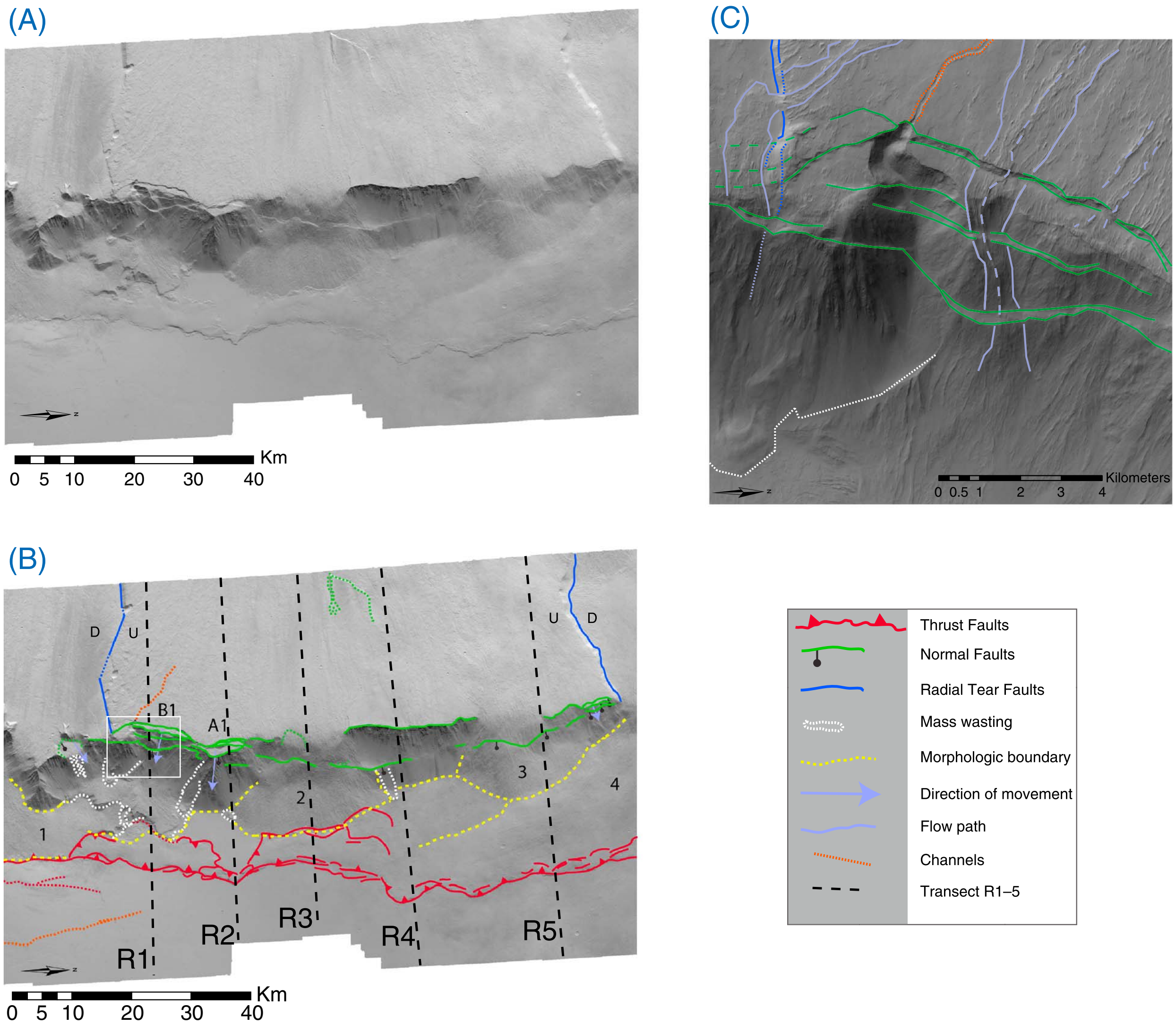

Figure 2. (a) Map view and (b) Structural mapping of the EOMBS from HRSC DTMs (75 m/pixel DTM, and 12.5 m/pixel image resolution) and (c) CTX image (5.6 m/pixel) of region B1 (indicated by white box) from Figure 2b. Contractional wrinkle ridges are shown as red lines, extensional normal faults are indicated by green lines, and radial tear faults are marked by blue lines, with U (up) and D (down) signifying the relative vertical motion. Dashed lines indicate uncertain expressions of fault traces, and fault markers (ball-and-stick on downthrown side of normal faults, and triangles on overthrust side of compressional faults) indicate inferred direction of relative movement. Areas of small mass-wasting events are indicated through dashed white lines, morphologic boundaries are shown by dashed yellow lines, channels are dashed orange lines, flow boundaries, and strongly pronounced individual flow striations in Figure 2c are indicated by purple and dashed purple lines, respectively. Flow and slump events are indicated by purple arrows, and "breached lava flows" (see section 2) are indicated by numbers 1–4. Letters indicate areas of specific interest: A1 indicates a large slump event (see section 2), B1 (see Figure 2c). HRSC DTM data product 1089_0000 (with resolutions of 75 m/pixel in the DTM, and 12.5 m/pixel in the image, processed through HRSCview: Freie Universitaet Berlin and DLR Berlin, http://hrscview.fu-berlin.de/). CTX image P11_005256_1985_XN_18N129W has a resolution of 5.6 m/pixel resolution.

locations are consistent with a landslide model, and flank stability minima are best satisfied by the occurrence of a dipping overpressured confined aquifer and mechanically weak sublayer at depth beneath the edifice. We also discuss implications for the structure of the edifice and formation of the aureole lobes through time.

2. Structural Observations and Characterization

We use three-dimensional HRSC DTM data product 1089_0000 [*Gwinner et al.*, 2007, and references therein] (DTM and image horizontal resolutions of 75 m and 12.5 m, respectively; Figures 2a and 2b) supplemented by Context Imager (CTX) data [*Malin et al.*, 2007] (5.6 m/pixel horizontal resolution; Figure 2c) to map the region of the east flank. The EOMBS exhibits two structures that are slope parallel to subparallel

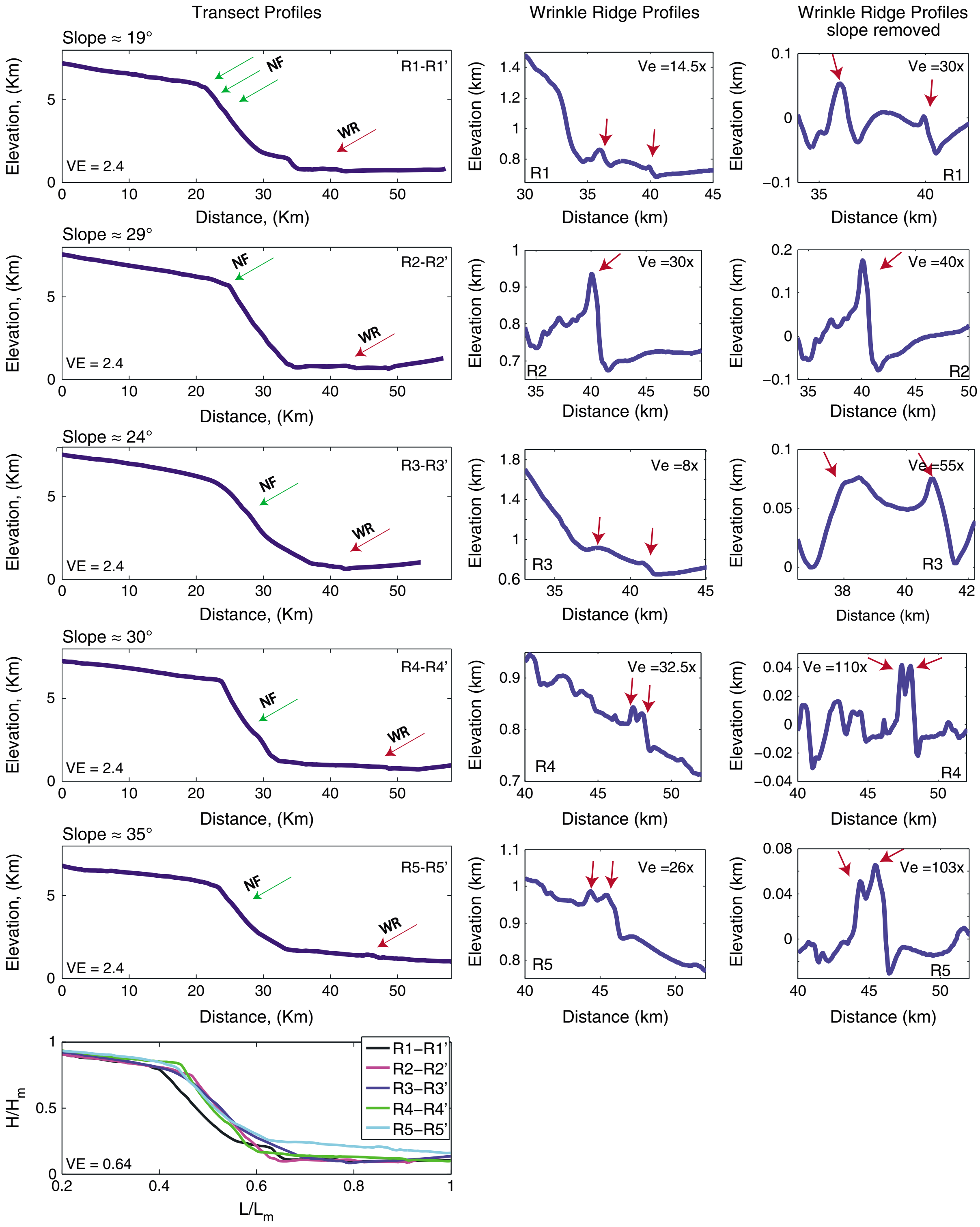

Figure 3. Elevation profiles of transects (Figure 2b), with the positions of normal faults (NF) and wrinkle ridges (WR) marked. Normalized elevation traces with values H/H_m versus L/L_m (where H is the height, L is the base length, and $_m$ is maximum extent) are shown for all profiles. Vertical exaggeration (VE) for all profiles is ~2.4 times. WR profiles and along-strike variation are generated from the topographic profiles with regional slope included (center column) and removed for clarity (right column). Red arrows indicate bounding faults.

bounding much of this region of the edifice (Figures 1c, 1d, 2a, and 2b). The length of the near-continuous upslope fault trace is ~100 km (green lines; Figure 2b). Observed offsets along the upslope on-scarp fault system are on the order of 10–100 m, with a normal sense of slip. The DTM resolution of 75 m is insufficient to directly sample and measure many of the offsets; however, offsets can be estimated using visible faults in the HRSC image, and the resolution of the HRSC DTM (~12–75 m). This system is bounded on either side by radial tear faults [*Borgia et al*., 1990] (blue line) that cut both the scarp face and the recent lava flows [e.g., *Basilevsky et al*., 2006].

The downslope fault network is 160–200 km long (red lines) and modifies the slope adjacent flows and plains through broad arches and crenulations. Along-strike variations for the 5 transects in the study region are shown in Figure 3. Observed offsets of the wrinkle ridges (measured from trough-to-ridge height) are on the order of 100 m. Individual smooth plain structures in the study area to the north (e.g., R4 and R5) have offsets on the order of 10–100 m. These results suggest that the upslope and downslope systems are normal faults and wrinkle ridges, respectively, consistent with the findings of *Borgia et al*. [1990].

While the maximum scarp slopes indicated in Figure 1c may reach values as great as 51°, this occurs only over a small region of the scarp itself, with average slope values, measured from the upper plateau to the lower plains (terminating at the wrinkle ridges), ranging from 19 to 35° (Figure 3) with the northern transects (R4 and R5) steeper than the southern transects (R1–R3). The normalized length-to-height slope profiles are normalized to a fixed upslope point and the shortest downslope transect distance (R3) in order to isolate the profile of the basal scarp. These results show a remarkably uniform basal scarp, despite the variance that is shown in Figures 1c and 1d. The toes of the slope show more distinctive and varied morphology, likely due to modification of the slope toe and adjacent smooth plains by lava flows and small, localized slope failures.

Several regions of the edifice show lava flows modifying the basal scarp. These flows often interact with the normal faults that are ubiquitous along the upper slope (region B1 Figures 2b and 2c). The crosscutting relationships between the flows and normal faults appear complex, with flow paths both covering and cut by normal faults (Figure 2c). Additional lava flows can be seen to overprint the fault trace of the southern radial tear fault (Figure 2c, bottom) and the cliff face of the EOMBS, before terminating at a lower elevation normal fault, suggesting that the normal faults in this area cut both the radial tear fault and the lava flows. This implies that the radial tear fault has not been active in this portion of the edifice since the age of the last flow and that at least some of the flows and normal faulting may have been contemporaneous (~200 Ma) [*Basilevsky et al*., 2006].

From limited exposures of layering along the edifice, flow thicknesses of ~6–100 m scale are evident. Several regions of the edifice exhibit what are inferred to be large volumes of breached lava flows that breach the upslope plateau and copiously cascade down onto the smooth plains (yellow dashed lines; Figure 2b). These regions of voluminous outpouring show clear continuous flow striations that extend from the edifice plateau and continue to the leading edges of the lobes along the smooth basal plains. Flow lobes in the central portion of the study area (2 and 3 in Figure 2b) are cut by normal faults, and lobes 1, 2, and 4, appear to be modified at their base by the wrinkle ridge network along the smooth plains. Lobes 1 and 2 are partially overridden by lower plain material associated with thrusting by wrinkle ridges of varying vergence (indicated by triangle notation; Figure 2b), which define the boundaries of pop-up structures.

The southern portion of the EOMBS shows evidence for small-scale slope failures, and possible landslide deposits (white dashed lines; Figure 2b). Additionally, larger-scale slumps appear to have occurred (arrows; Figure 2b). Each failure is characterized by multiple arcuate normal faults along the headwall and either large debris aprons or downthrown blocks along the scarp face. The largest slump occurs adjacent to lobe 2 (A1 in Figure 2b). Failures appear more developed in the southern portion of the study area. Increased offsets along the wrinkle ridges, preferential deposits of landslide debris, and slump blocks in the south of the edifice suggest past, small-scale, flank instability. The southern portion of the EOMBS may therefore be more unstable and consequently have a greater chance of slope failure.

We suggest that the two identified fault systems bound a volume of material that has the potential to fail as a coherent landslide through a linked failure surface. This failure requires the upslope fault system to be extensional, and the downslope faults to be contractional. Both the normal faults and wrinkle ridges record similar amounts of offset, suggesting that overall deformation of the Olympus Mons eastern flank may be accommodated by both fault systems in concert. The downslope faults along the plains units can be inferred to be the bounds of pop-up structures, the formation of which suggests the existence of a detachment zone at depth. Using topographic data and limit equilibrium approaches, we attempt to estimate the depth of the failure surface required to match the physical expressions of deformation along the EOMBS, to test a landslide-related origin for the basal scarp and adjacent aureole lobe.

3. Slope Stability Approach

Our ability to carry out detailed analyses of structural features and slope failure mechanisms has been made possible by the availability of high-resolution HRSC DTMs [e.g., *Gwinner et al.*, 2007]. To carry out the analyses, profiles along the basal scarp, perpendicular to the interpreted fault traces, are analyzed to estimate the stability of the slope, given by the Factor of Safety (F_s). The F_s is the ratio of resisting to driving forces within the slope and is determined using limit equilibrium methods.

Broadly, a $F_s \gg 1$ implies that resisting forces are greater than driving forces for the chosen failure surface and material properties, and the slope is considered stable. Conversely, a $F_s < 1$ suggests that driving forces are greater than the resisting forces, and the slope state is considered unstab. A $F_s \approx 1$ arises when resisting and driving forces balance, and the slope is considered critically stable. The slope could either fail or become stable given minor changes to any parameter.

The limit equilibrium approach, explicitly assumes that the material at failure obeys the Mohr-Coulomb criterion [e.g., *Fellenius*, 1926; *Terzaghi*, 1946] and is a powerful tool for assessing slope stability. There are many different limit equilibrium approaches (see *Anderson and Richards* [1987] for a review of these approaches), but they must all satisfy overall force equilibrium, overall moment equilibrium, or both. Given uncertainties inherent in remote sensing data sets (e.g., unknown subsurface structure, material properties, etc.), we focus our analyses using methods that minimize the number of unknowns. Given the previous uncertainties, we use the less rigorous overall static force equilibrium approach of Janbu's simplified method [*Janbu*, 1954] and of the simple Wedge method [e.g., *Anderson and Richards*, 1987] (hereto simply referred to as Janbu's, and Wedge methods, respectively) to probe flank stability.

Janbu [1954] published one of the first routines for the analysis of a noncircular failure surface, although it is easily adapted to circular geometries (as has been done for this work). This method uses a force equilibrium approach, and assumes that both the moment equilibria and the sum of the interslice shear forces (shear force along a discretized, or slice, boundary) can be neglected. Janbu's method is nonlinear and iterative. The method can be strongly overdetermined, and it should be verified against other methods to check for consistency.

The Wedge method is among the simplest of limit equilibrium approaches and is particularly useful if there is a weak stratum included within or beneath the slope [*Anderson and Richards*, 1987]. As the name implies, the geometry assumed for this method is that of a simple wedge. Its linear approach requires few assumptions, and as a result, may avoid becoming overdetermined. Due to its explicit calculation the resulting F_s is likely to have greater errors and may tend to overestimate F_s when compared to Janbu's method. Thus, we assume the actual F_s value as likely to fall between the two methods' results.

The constitutive equations for the two methods we use are:

$$F_{s-\mathrm{Janbu}} = \frac{\sum\left(\mathrm{cl} + \left(P_{\mathrm{Janbu}} - \mathrm{ul}\right)\tan\phi\right)\sec\phi}{\sum W\tan\alpha} \tag{1}$$

and

$$F_{s-\mathrm{Wedge}} = \frac{\sum\left(\mathrm{cl} + \left(P_{\mathrm{Wedge}} - \mathrm{ul}\right)\tan\phi\right)}{\sum W\sin\alpha} \tag{2}$$

where P_{Janbu} and P_{Wedge} are given by:

$$P_{\mathrm{Janbu}} = \frac{\left[W - {}^{1}/_{F_s}\left(\mathrm{cl}\sin\alpha - \mathrm{ul}\tan\phi\sin\alpha\right)\right]}{\left[\cos\alpha\left(1 + \tan\alpha\,{}^{\tan\phi}/_{F_s}\right)\right]} \tag{3}$$

and

$$P_{\mathrm{Wedge}} = W\cos\alpha \tag{4}$$

defining the normal forces acting on a slice, or discretized planar element along slip surface (assumed to act on

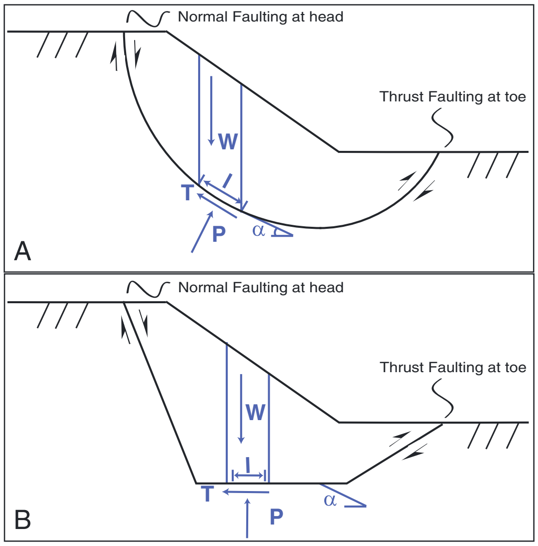

Figure 4. Idealized slip surface geometries and methods for calculating the Factor of Safety (F_s) using (a) Janbu's and the (b) Wedge methods, where W = slice weight, T = resisting force acting on a slice, α = angle from horizontal to failure surface, P = normal force acting on a slice, and l = length of slice along the failure surface.

the center of each slice's base), u is the pore fluid pressure (where $u = \rho_{\text{water}} gz$, with ρ_{water} the density of fresh water, g is martian gravity, and z is depth below the surface), c is the cohesion, ϕ is the angle of internal friction, W is the weight of the overlying material, l is the length of the slice along the failure surface, and α is the angle from the horizontal to the failure surface. The equations are calculated for n discrete slices over the slope volume. The nonlinearity in F_s for Janbu's method (equations (1) and (3)) requires an iterative solution. An initial assumption of independence on F_s is assumed, and the method is iterated until the convergence criterion is satisfied to account for the nonlinearity of equation (3). A discussion of the specific mechanics of the convergence criterion and iterative methods used can be found in any nonlinear solver textbook [e.g., *Kelley*, 1995]. A simple schematic view of both the geometries and variable definitions are given for Janbu's (Figure 4a) and the Wedge methods (Figure 4b).

We estimate F_s for a range of possible slope configurations. We first define a set of upslope and downslope points that delineate the region that slip surfaces will be generated within. Within the bounds of the starting and ending points, a series of nodes are generated connecting the upslope to downslope regions via linked failure surfaces (mesh) of differing depths (Figure 5a). The initial slip surface between nodes is defined to give the maximum radius possible (greatest depth of the slip surface). The radii of this circle is then decreased (shallowing of the failure surface), under the conditions that each node considered falls on the circumference of the circular slip surface for all radii, and the slip surface cannot breach the surface of the slope between the nodes considered. For Janbu's method the circular geometries are unmodified, and for the Wedge

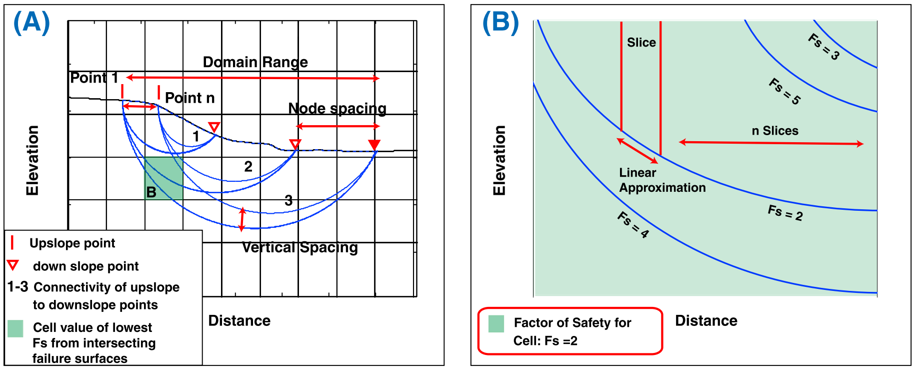

Figure 5. (a) A generalized example of the slope stability search method is shown. While the circular geometries that are used with Janbu's method are indicated, the method is easily adapted to the noncircular geometries of the Wedge method. Potential slip surfaces (blue lines) are generated by linking upslope nodes (constrained within the region of Point 1–Point n) to each successive downslope node via a range of linked radii, with a sampling rate controlled by the user-defined nodes and vertical spacing criteria. The results are displayed as cells and are assigned the value of F_s for each potential slip surface that intersects that cell. In the case of multiple F_s intersecting a particular cell, the lowest F_s is selected and the cell assigned that value (the green cell labeled "B"). (b) A close-up of the green cell in Figure 5a. Multiple slip surface with differing values for F_s and the discretization of the slip surface via individual slices are shown.

Table 1. Layer and Sublayer Model Properties[a]

Model		Water Present	Density (kg/m^3)	Friction Angle (deg)	Cohesion (MPa)	Water/Layer Boundary Location (km)
M1	Homogeneous	Dry	3000	30	4	––
M1A	Homogeneous	Free Standing	3000	30	4	4
M2	sublayer	Dry	2200	30	0.3	4.7–5.7
M2A	sublayer	Aquifer	2200	30	0.3	4.7–5.7
M3	sublayer	Dry	2200	30	0.3	−0.5–0.5
M3A	sublayer	Aquifer	2200	30	0.3	−0.5–0.5
M4	sublayer	Dry	2200	30	0.3	−2.5–3.5
M4A	sublayer	Aquifer	2200	30	0.3	−2.5–3.5
M5	sublayer	Dry	2200	30	0.3	−4.5–5.5
M5A	sublayer	Aquifer	2200	30	0.3	−4.5–5.5

[a]Sublayers (models M2–M5) are regions of different mechanical rock properties contained within the homogeneous rock mass of M1.

method the circular failure geometry is modified to a wedge geometry. The slip surface is then discretized into *n* number of slices, with *n* chosen to ensure that each slice intersects a cross section of the failure surface that may be sufficiently small to approximate a linear slope (Figure 5b). We systematically test the stability of all portions of the slope by assigning both node spacings (horizontal resolution) between slope points, and slip surface spacings between failure radii (vertical resolution), creating a mesh of overlapping runs, or a “bird's nest” of failure surfaces. The nominal horizontal node spacing is selected to be on the order of 75 m, the resolution of the HRSC DTM, and the vertical mesh spacing is selected to be on the order of 100 m. These values allow for between 1×10^4 and 1×10^6 individual slip surfaces to be generated per model, per transect along the slope. The overlapping resultant slip surfaces are subsequently gridded into cells, with each individual cell assigned the lowest F_s passing through its domain (Figure 5). The cell gridding of the stability minima indicates coherent regions of consistently low F_s, suggesting that lower stability failure surfaces are more likely to pass through these sectors of the gridding space given the topography of the system and the geometries employed. While slip surfaces that are more resistant to failure will also pass through these sectors, they would likely not be the slip surfaces where slope failure would initiate and are not favored in our routine. Cell gridding allows for coherent and self-consistent regions of low F_s, from multitudes of individual slip surfaces, to be easily determined, independent of initial choices for slope geometries.

3.1. Model Stratigraphies

Subsurface stratigraphy and strength variations can influence the F_s stability [e.g., *Anderson and Richards*, 1987]. Given the absence of subsurface observations for Mars, we test a range of plausible configurations and calculate the resulting F_s values. Spectroscopic evidence for the existence of phyllosilicates at the surface of Mars [*Bibring et al.*, 2006] provides support for the existence of a décollement that accommodates basal spreading of Olympus Mons [e.g., *McGovern and Morgan*, 2009]. While phyllosilicate layer thicknesses are unknown, to minimize the number of variables we assume these layers to be on the order of 1 km thick. We consider the effects of thinner and thicker layers in the supporting information.

Several edifice stratigraphies for each of the previously defined transects (R1–R5) are tested to match observed faulting locations: (1) a homogeneous rock mass and (2) a weak 1 km thick sediment (i.e., phyllosilicate) layer placed within the edifice at an elevation of 4.7 km (~ 2 km below the shield plateau, within the basal scarp), and at 0, 3, and 5 km below the global reference datum. Throughout the paper, the term “weak” refers to a layer of low cohesion material. Each stratigraphic model is run for dry (no pore fluid pressure, $u = 0$) and hydrostatic pore fluid conditions ($\lambda \approx 0.3$–0.4, where λ is the pore fluid pressure ratio, defined as $u/\rho_{\mathrm{rock}} gz$, and a value of $\lambda = 1$ is lithostatic). The effects of pore fluids are resolved at the slip surface interface. The force balance, taking into consideration pore fluid pressure and density, is summed over *n* slices. Additionally, substrates that dip toward the edifice are considered to emulate flexural effects [e.g., *Morgan and McGovern*, 2005]. Model properties are summarized in Table 1 and outlined in Figure 6.

3.2. Mechanical Properties of Models

Models 1 (M1) and 1A (M1A) considers two end-member cases: M1 is setup with dry homogenous properties whereas M1A features water present in the pore spaces throughout the subsurface up to 4 km elevation [e.g.,

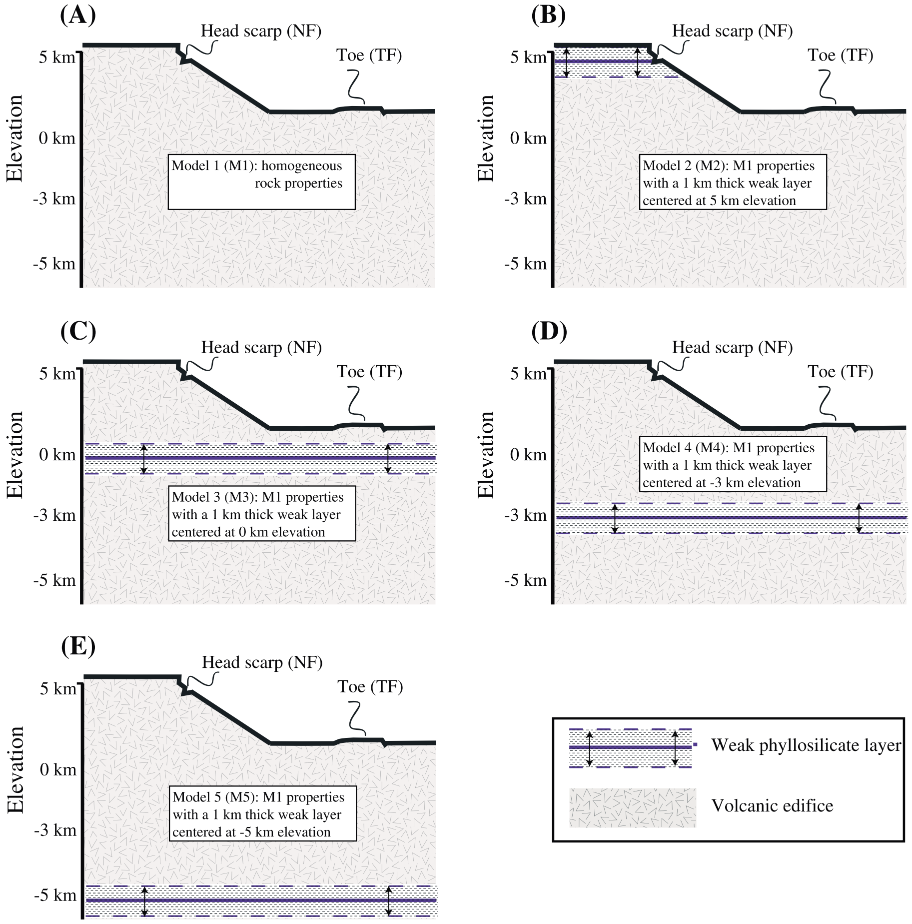

Figure 6. (a–e) Schematic diagram of models M1–M5 showing the central location of a weak layer (blue line), the extent of the layer above and below the center point (double-headed arrows), and the relevant layer depth within the edifice. For simplicity, these models contain two materials: a mechanically weak sublayer and homogeneous volcanic rock mass.

Fairén et al., 2003] along the 7 km high scarp. Both end-member cases include a homogeneous rock mass with cohesion of 4 MPa and an angle of internal friction at 30°, consistent with Hawaiian layered effusive basaltic volcanics [*Okubo*, 2004]. We assume a rock mass that is pervasively jointed, fractured, and layered, with $\rho = 3000$ kg/m^3. This value is lower than that reported for the overall density of 3200 kg/m^3 obtained by *Lodders* [1998] for intact Martian basalts but greater than values reported for effusive Hawaiian volcanics [e.g., *Okubo*, 2004] to account for the higher density of Martian basalts. However, the effects of different densities are negligible given the uncertainties in the datasets; a density difference of ±200 kg/m^3 results in a change in F_s on the order of 1% (see supporting information). The density of water, if present, is 1000 kg/m^3, and at hydrostatic pressure unless otherwise noted.

Model 2 modifies M1 with a weak 1 km thick stratigraphic layer that is dry (for model M2) and containing pore fluid (for model M2A). This layer is placed upslope within the EOMBS at an elevation of 4.7–5.7 km above the global reference datum. To test the effects of isolated pore fluids (in contrast to the inundated conditions outlined for M1A), the pore fluid in M2A is confined from the top of the weak stratigraphic layer to the base of the model domain. The weak layer has a cohesion of 0.3 MPa, an angle of internal friction of 30°, and a density of 2200 kg/m^3, roughly consistent with the physical and mechanical properties of a weak shale layer [e.g., *Goodman*, 1989], which is analogous to the sedimentary Burns Formation at Meridiani Planum [*Nahm and Schultz*, 2007]. Given the uncertainties in the data sets, a conservative higher value for the angle of internal friction of the weaker sublayer was chosen. While the magnitude of F_s is influenced by decreasing the angle of internal friction (a decrease of 5° from the

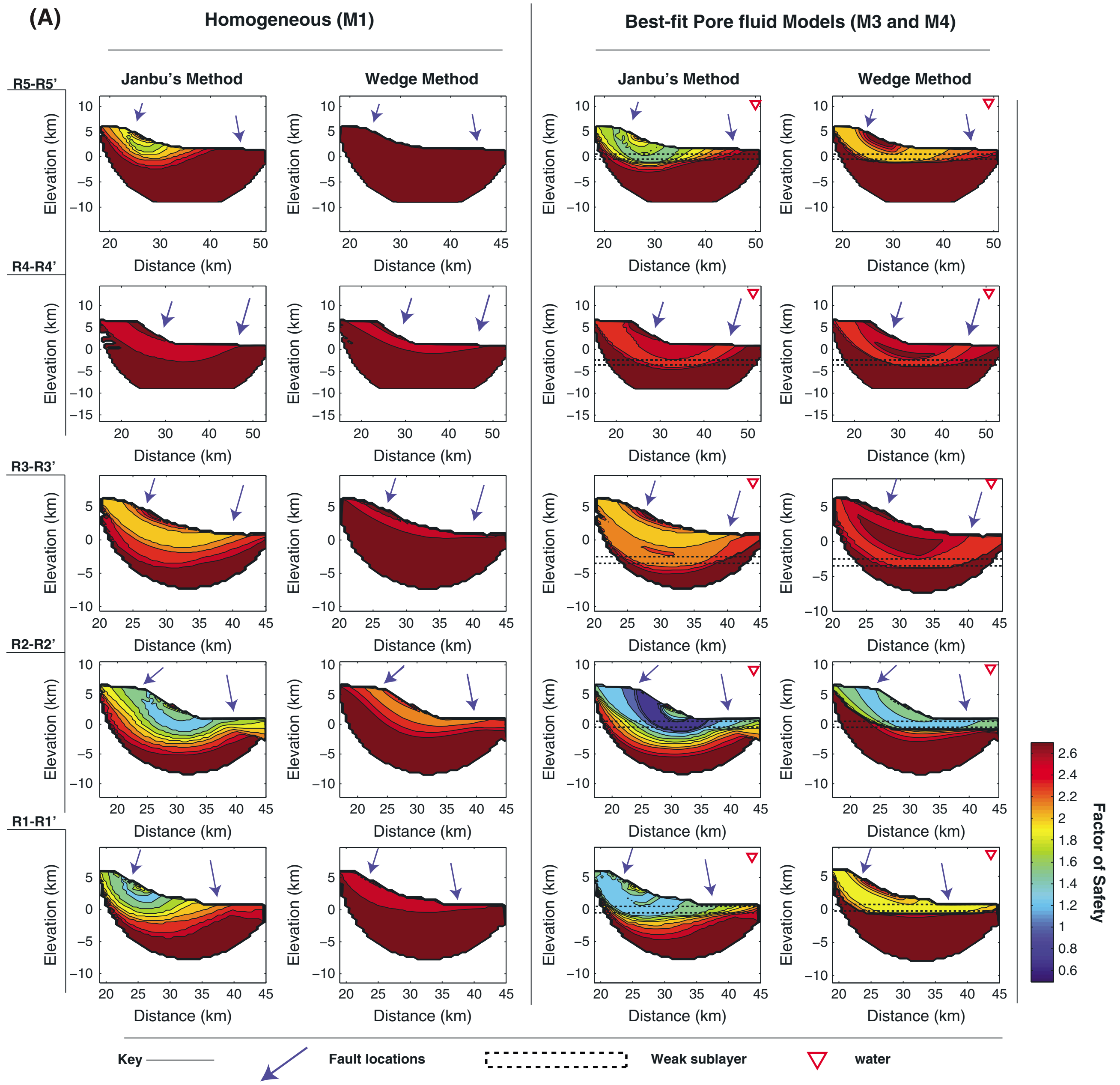

Figure 7. (a) Slope stability search results for Janbu's and Wedge methods for the dry homogeneous reference case M1 for (left 2 columns), and best fit models including a weak sublayer and nominal pore fluids for each transect, and for M2A–M5A (right two columns) are considered. Only the single best-fit model per transect is shown. Contours show regions of low Fs using the search algorithm outlined in Figure 5. Blue arrows indicate the location of faults; a red triangle indicates presence of hydrostatic pore water within a confined aquifer. (b) Expanded view of model M3 for transect R1 using Janbu's and the Wedge method. Failure surfaces with the lowest F_s (red dashed lines), from the search algorithm outlined in Figure 5, are plotted on the overall F_s contour plots, highlighting the similarities and the differences in derived failure surface geometry and F_s between the models. In the case of Janbu's method, an inslope restricted upper (ub) and lower (lb) branch F_s is indicated.

reference rock mass value of 30° to 25° leads to a maximum of ~13% difference for Janbu's, and ~5% difference for Wedge results), the geometry of the failure surface itself is largely unaffected (see supporting information). The remaining parameter space is explored by decreasing the layer depth, defined as depth of the layer's midpoint, to 0 km (for model M3), −3 km (for M4), and −5 km (for M5) for dry conditions (and corresponding models M3A, M4A, and M5A, respectively, for confined aquifer conditions), relative to the global reference datum.

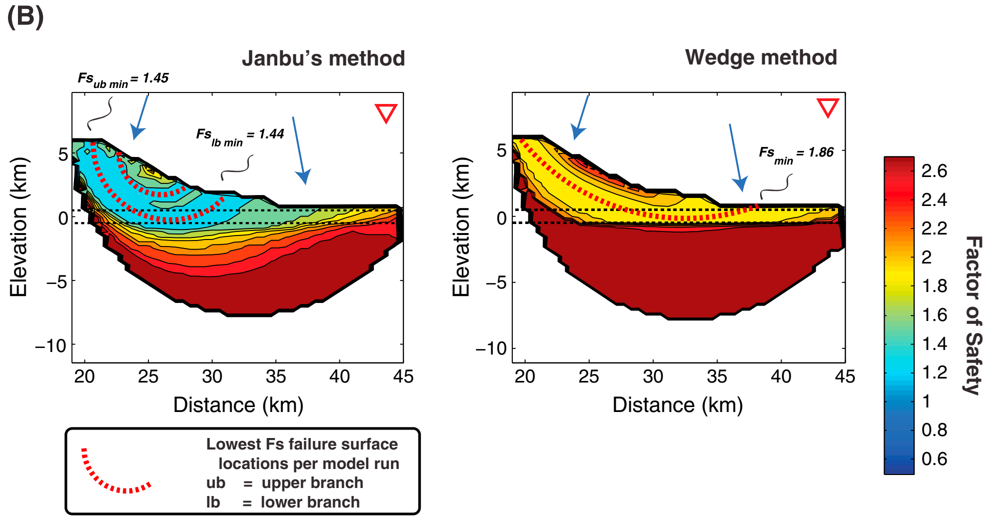

Figure 7. (continued)

Models with an overpressured (i.e., greater than hydrostatic pressure) confined aquifer are also considered. In these models, overpressurization of the aquifer to the deep layer cases is restricted at −3 and −5 km below the edifice (for models M4OP and M5OP) to ensure that the aquifer would not be in contact with the surface, as the placement of the water table in models M1, M2, and M3 may allow. The maximum pore fluid pressures permitted in our models are superlithostatic ($\lambda = 1.6$). This maximum would likely be associated with rapid tectonic events that could lead to a rapid increase in pore pressure over very short timescales. The stresses involved would not be supported by the edifice over any appreciable length of time, leading to the fracture of the rock mass, and the immediate loss of water [e.g., *Hanna and Phillips*, 2006].

4. Factor of Safety Analysis of the EOMBS

We calculate F_s to examine edifice stability based on structural models and previous interpretations of the edifice [e.g., *Basilevsky et al.*, 2006; *McGovern and Morgan*, 2009]. Contour plots from slip surface geometries and minimum F_s search routines define coherent regions of low F_s that may be inferred to be the potential failure region. Each grid cell, and consequently contour, from the search routine represents the influence of many individual failure surfaces, and not a single discrete failure plane. This approach is weighted toward lower F_s on the principle that slopes are only as strong as their weakest constituent, and initial failures will preferentially occur within weak regions. As multiple low F_s slip surfaces intersect within a region of the edifice, the probability that failure would occur at this location becomes enhanced within our model space. While higher valued F_s also intersect in these regions, the failure surface would be unlikely to utilize the higher F_s slip surfaces. The results summarized in Figures 7 and 8 (and the supporting information for individual model runs) may be considered regions of higher failure potential for a given set of individual model parameters. Each of the models are tested for transects R1–R5. We compare the results of Janbu's and the Wedge methods to assess the stability of the Olympus Mons edifice.

4.1. EOMBS Without a Preexisting Weak Layer

The reference case of M1 is shown for Janbu's and the Wedge methods (Figures 7a and 7b). All modeled transects indicate that the identified faulting locations from mapping occur in regions of high F_s (> 1.6). From Janbu's method the southernmost transects R1 and R2 indicate the lowest overall F_s (~1.2–1.45). F_s increases toward the central and northern regions of the edifice for transects R3 and R4 ($F_s > 2$), before showing a decrease in the northern edge of the system (shown in transect R5, with a $F_s \sim 1.6$).

The Wedge method generally predicts geometries similar to those determined from Janbu's method, although the former approach favors broader (less small-scale variation) contours, and indicates greater

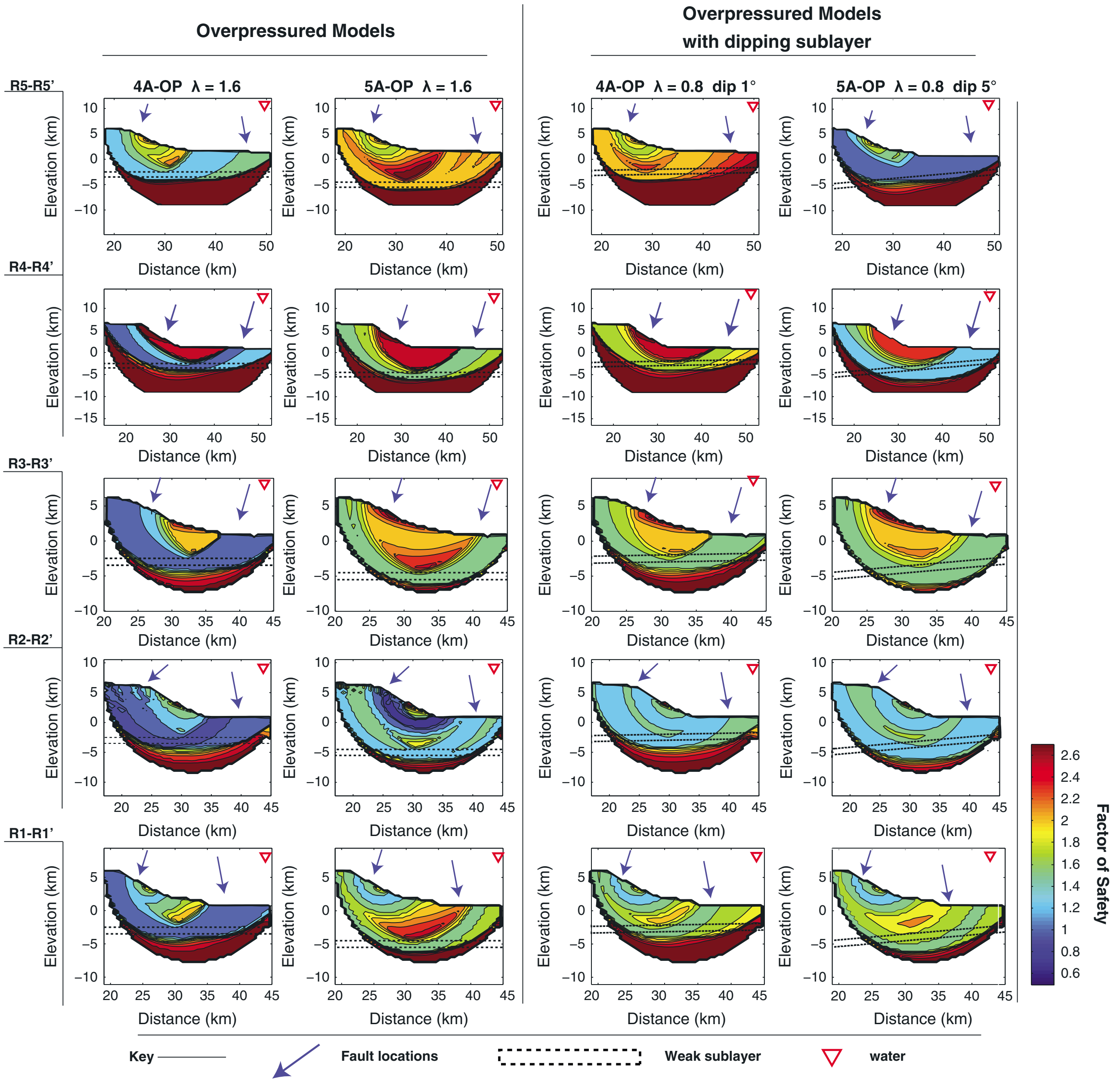

Figure 8. Slope stability search results for Janbu's method for deep (−3 km and −5 km) overpressured models M4OP and M5OP at $\lambda = 1.6$, and an overpressured dipping detachment at $\lambda = 0.8$, dipping toward edifice at 1° (M4OP) and 5° (M5OP). Contours show regions of low F_s using the search algorithm outlined in Figure 5. Blue arrows indicate the location of faults; a red triangle indicates presence of pore water.

values of F_s (~30% greater than Janbu's method). All transects are found to yield $F_s > 1.9$. All mapped faulting locations occur within broad regions of relatively low F_s, which largely consist of the entire near-surface portion of the edifice, leading to an inconclusive match for faulting locations.

The inundated water configuration (M1A) generally lowers the F_s values relative to M1 by ~30% but preserves the general pattern of F_s geometries for both Janbu's and Wedge methods through a reduction in relative density. These conditions, using Janbu's approach, predict that transects R1 and R2 would be in failure, and R5 would approach failure. In contrast, only transect R2 would be near failure following the Wedge method. However, similarly to the dry Wedge method results, predicted failure locations from the Wedge methods inundated water configuration are poorly matched to the mapped fault locations.

4.2. EOMBS With a Preexisting Weak Layer and Pore Fluid

We consider models including a weak substrate at varying depths. Model parameters for M1–M4 are summarized in Table 1. For clarity, results in this section are described in relation to M1; the individual model runs can be found in the supporting information. In general, for both methods, models under dry conditions show negligible changes of F_s from the reference case M1 (Model 1 shown in Figure 7a (left two columns)). The change in F_s between models, per transect from the reference case of M1, reaches a maximum of ~ -0.3 for M3, while F_s of M2, M4, and M5 are largely unaffected by the inclusion of a weak substrate. Moderate improvements in predicted versus observed fault geometries for M3 and M4 are suggested in the southernmost transects only (R1 and R2).

The inclusion of pore fluids has the greatest effect on M3 and M4. In M3A, using Janbu's method, transect R2 is critically stable ($F_s \sim 1$). Using this same method, transect R3 is at ~80–100% greater than critical stability, transect R5 shows a broad weakening of the slope by ~17%, and the agreement between faulting locations and F_s minima for both transects are largely unchanged from the reference cases. In contrast, the Wedge method results for M3A suggest that transect R2 begins to approach the critical value of F_s, but this region remains broad, whereas transects R3 and R5 begin to move toward conditional stability in the region of observed faulting.

Results from M4A for both Janbu's and the Wedge methods indicate that F_s values along observed faulting locations are largely unchanged from M1. However, the subsurface geometries for transects R1, R3, and R4 begin to show divergence, with a partitioning of regions of F_s along both a deep and shallow contour. This effect is greatly enhanced in the Wedge method results of R1–R4, showing a second, much deeper (at depth below the edifice) focused region of F_s minima at conditional stability that is in excellent spatial agreement with the observed locations of contractional faulting.

M2 and M5 show minimal deviation from the homogenous reference case (M1). All transects with sublayer thicknesses less than 1 km show negligible to no deviations from M1, whereas thicknesses of 5 km show minimal deviations from the 1 km case (see supporting information). These results indicate that a weak sublayer deeper than −5 km below the edifice base, a weak sublayer within the edifice slope, or a weak sublayer of less than 1 km thickness, will contribute only negligibly to the instability of the edifice and to the expression of the surface tectonics.

The best fit models described in the previous paragraphs include sublayers with pore fluid and produce both the lowest overall F_s and the best fault matches, shown for both Janbu's and Wedge methods (Figure 7a (right two columns)). The best fit detachment depth (or, as a proxy, sublayer depth) is determined from the lowest F_s value in the region of the observed faulting (lowest F_s contour at the location of blue fault arrows for both the extensional and contractional faults). Best fit depths occur at 0 km for transects R1 and R2, −3 km for R3 and R4, and 0 km for transect R5 for both Janbu's and the Wedge methods (Figure 7a). This geometry, under these assumed model conditions (pore fluid content, sublayer depths, mechanical properties, etc.) indicate a potential concave up geometry along the circumference of the edifice (transects R1–R5) for the detachment surface and sublayer depth, and is robust between methods (Figure 7b). While Figure 7a indicates increased goodness of fit for both a F_s approaching unity and matching upslope faulting locations, transects R3–R5 (the northern face of the eastern basal scarp) generally require deeper detachments in order to match the observed wrinkle ridge locations. However, it is much more difficult to explain the upslope normal faulting, and the greater stability of the edifice in the North. Other mechanisms such as overpressured pore fluid may be required for northern slope geometries to be explained through flank failure.

4.3. EOMBS Destabilization From Overpressure and Dipping Décollements

The previous section described a southern region of the eastern basal scarp at, or within, 30% of critical stability but a northern portion of the eastern basal scarp that can be considered conditionally stable. This section explores the potential mechanism of pore fluid overpressurization to weaken the slope such that a near-critical F_s may be recovered for regions of observed faulting along the entire eastern basal scarp.

The results for M4OP and M5OP (overpressured to the maximum pore fluid ratio of $\lambda = 1.6$ using Janbu's method) are shown in Figure 8 (left two columns). These results indicate that deeper sublayers can exert greater influence on slope stability if the water they contain is sufficiently overpressured (greater than hydrostatic). All transects in these models show an increased agreement between locations of wrinkle ridges and more narrowly confined regions of F_s minima relative to previous models (contrast Figures 7 and 8). Additionally, all F_s minima decrease relative to previous models: under an overpressured scenario, transects R1 and R2 are within 10% of critical stability, transect R4 is within 20%, and transect R5 is within 40%. Best fit layer depths for all transects and methods show a planar detachment depth of -3 km. Normal upslope faulting shows improved agreement from previous results with F_s minima for all transects but R4. This is unsurprising as much of the edifice has undergone some form of mass wasting and may be substantially modified.

The inclusion in these models of a sloping substrate, dipping 1° toward the edifice, lowers the F_s by ~ 30% for nominal pore fluid cases, with the agreement of faulting locations largely unaffected. A sloping substrate that is overpressured to $\lambda = 0.8$ in M4OP, M5OP (Figure 8 (right two columns)) and dipping 5° toward the edifice at a depth of -5 km predicts a slope near failure. Increasing the dip allows for sublayers at greater depths to increasingly influence the surface tectonics. In general, the inclusion of overpressured pore fluid and a dipping substrate show marked improvements between the locations of F_s minima and observed faulting locations, as well as a pronounced decrease in flank stability.

5. Discussion

The results described above show that limit equilibrium analyses can account for observed faulting locations along the edifice. The locations of the normal faults and wrinkle ridges can generally be linked through a failure surface if the edifice is underlain by a weak, relatively thin (~1 km thick) sublayer that has mechanical properties consistent with that of a mechanically weak layer (possibly phyllosilicate) acting as a confined aquifer. The best agreement between observed faulting locations and the location of a failure surface that describes a critically stable slope is found with an overpressured ($\lambda = 1.6$) sublayer that is horizontal, or with a gently dipping (i.e., 1–5°) sublayer at lower overpressures ($\lambda \sim 0.8$).

5.1. A Comparison Between Methods

While both Janbu's and the Wedge methods generally report similar results, there exist differences as well. Janbu's method results in F_s values that are typically ~25% lower than those reported for the Wedge method and tend to provide relatively poor matches to the observed wrinkle ridge locations. While both Janbu's and the Wedge methods can indicate a partitioning of F_s minima into both shallow and deeper regions (e.g., Figure 7a), the Wedge methods partitions (transects R3 and R4 best fit models Figure 7a) tend to occur at much more shallow depths along the slope (near surface), and at much greater depths below the edifice (~ -5 km) than the partitioning of the Janbu method (Figure 7b). The Wedge results can match both locations of faulting well, with the normal faults occurring at the shallow portions, and the wrinkle ridges occurring over deeper failure surfaces. This second, deeper region of low F_s occurs from the effects of the mechanically weak sublayer, which extends the likely region that contractional faulting would occur out from the edifice. As Figure 8 shows, invoking significant overpressures and/or dipping décollements allow for Janbu's method to become increasingly sensitive to the effects of the sublayer.

Structural mapping may provide an explanation as to why two discrete regions of low F_s exist for Janbu's method. Figure 2b along transect R2 shows a large block of material has partially collapsed (downdropped block A1; Figure 2b). From the mapping it is apparent that there is a shallow (along-scarp) slip surface along which the block has moved. This shallow slump is in contrast to the much larger, deeper seated edifice slip surface that can be seen in transect R2 for the M3A, M4A, and OP models (Figures 7 and 8). Janbu's method appears to preferentially capture the shallower slump failure (Figures 2 and 7), while the Wedge method appears to be relatively insensitive to these small-scale failures, and instead favors the identification of the deep-set large-seated failures, that have higher F_s associated with them, with the notable exceptions of transects R3 and R4 in Figure 7a (right two columns).

These results indicate that for any slope failure, there are likely to be several nested slip planes in operation during the failure process, and these slip planes may record multiple failure events. A single slope stability approach, with its distinct set of assumptions, and a single discrete failure plane, may be insufficient to capture all potential slip surfaces, and as a result, multiple slope stability approaches may be required.

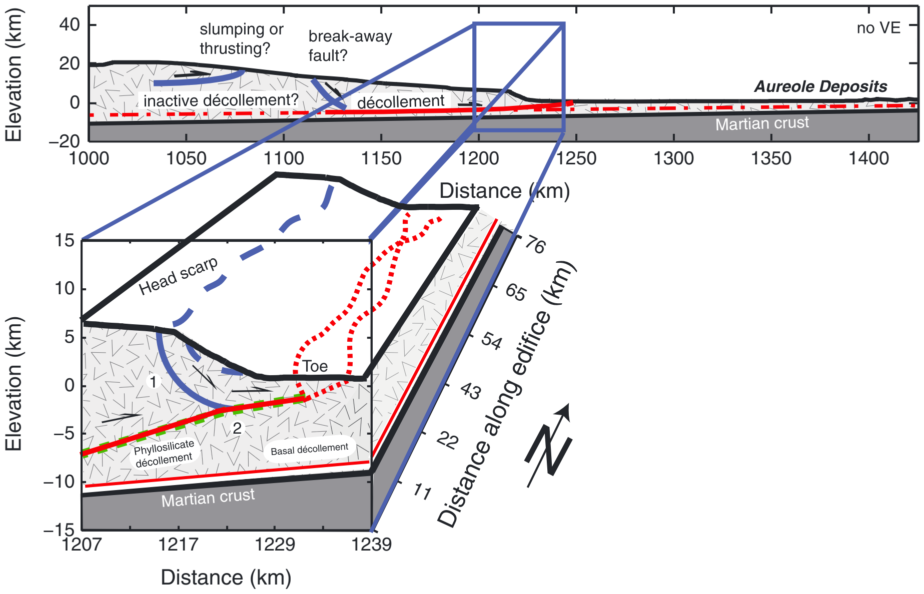

Figure 9. Cross-sectional view of Olympus Mons as a spreading volcano [after *Morgan and McGovern*, 2005], with a schematic structural interpretation of the EOMBS. Slope failure may take advantage of the preexisting phyllosilicate basal detachment, through a shallow branch of this deeper detachment nearing the surface, as suggested by pop-up structures (Figure 2). The model results allow for a plausible range of detachment depths (0 to −5 km). Portions of the slope marked by 1 (above −3 km; models M1–M3) indicate where pore fluid pressure may be the significant factor in destabilizing the slope (denoted by solid lines) and matching the observed fault locations. Portions of the slope marked by 2 (below ~ −3 km; e.g., M4) indicate where nominal pore fluid pressures are insufficient alone to destabilize the slope or match the observed faulting locations (dashed lines), instead requiring overpressures to superlithostatic pressures. For these detachment depths, normal fault bifurcations occur, and portions of the edifice remain conditionally resistant to failure under the conditions of a horizontal décollement and sublithostatic pressures.

5.2. Implications for the Edifice Structure

Morgan and McGovern [2005], *McGovern and Morgan* [2009], and *Byrne et al*. [2013] found the structural geometries of Olympus Mons are largely consistent with that of a spreading volcano. Their interpretations require that Olympus Mons is underlain by a relatively thin and weak stratigraphic unit, consistent with the presence of a layer of phyllosilicates consistent with spectroscopic detections of phyllosilicates presented in *Bibring et al*. [2006]. We consider it likely that such a layer is emplaced into lowland areas from higher adjacent terrain such as the Tharsis Rise and along the hemispheric dichotomy boundary. However, the only large volcanoes that were emplaced on such a layer were Olympus Mons and perhaps Apollinaris Patera the two Martian volcanoes with prominent basal scarps and flanking disrupted terrain. The other large Martian volcanoes were likely too high in basal elevation to have substantial thicknesses of sediments at their bases (e.g., Tharsis Montes and Alba Mons). The results of this work are in agreement with the assertions of *McGovern et al*. [2004a] and *McGovern and Morgan* [2009], who concluded the existence of pore fluid underneath the edifice is required to match observed fault locations. Models that do not include pore fluid fail to reproduce many of the observed faults along the transects, and this work further suggests that nominal pore fluid pressures alone are insufficient to match observed faulting geometries. We find that models that include pressures in excess of lithostatic ($\lambda = 1.6$) with a flat substrate, or sublithostatic ($\lambda = 0.8$) with a dipping substrate, can greatly improve, and in most cases match to observations, the predicted locations of faulting, where the lowest overall F_s values occur (Figure 8). Pore fluid overpressures allow for deeper detachments depths along the transects. However, superlithostatic pressures would be short lived, with pore fluids escaping from the edifice catastrophically. The release of groundwater, perhaps coincident with the deformation of the eastern basal scarp adjacent wrinkle ridges at < 50 Ma, could potentially form the estimated 25–40 Ma extensive channel networks adjacent to and to the south of the eastern basal scarp (the periphery of this network is indicated by channel along the basal plains in the SE corner Figure 2a and 2b) [*Basilevsky et al*., 2006].

The morphology of this unique portion of the Olympus Mons edifice, the EOMBS with its slope-parallel normal faults and wrinkle ridges, is consistent with the existence of a thin basal detachment, suggested from models of Olympus Mons as a spreading volcano [*Morgan and McGovern*, 2005; *McGovern and Morgan*, 2009; *Byrne et al*., 2013]. Our models allow for its depth, thickness, and material properties to be estimated. Verification of the existence of a basal detachment, with a minimum thickness of 1 km and mechanically consistent with a phyllosilicate stratum, allows for insights into the development of Olympus Mons in a number of ways. (1) The presence of a basal detachment allows for the edifice to spread laterally, modifying slope geometries and consequently slope stabilities through time; and (2) a basal detachment, linked to, and a consequence of a spreading edifice, allows for the development of a zone of failure that bounds a significant amount of material, with direct implications for the formation via (catastrophic) collapse of the aureoles.

A cross-sectional view of the eastern edifice interpreted by *Morgan and McGovern* [2005] is reproduced, modified, and expanded upon in Figure 9. This model invokes a gently dipping, possibly inactive, basal décollement extending away from the edifice, from which a secondary décollement, along which spreading may occur, daylights at roughly the same location as the observed wrinkle ridges. Our models suggest the detachment underlying the wrinkle ridges occurs at ~ 0 km elevation, with detachments 5 km below the edifice favored for systems with overpressured pore fluid and inclined weak strata. The geometry of the detachment along the edifice, derived from best fit models (Figures 7 and 8), is generally concave up for nominal pore fluid pressures, and horizontal for overpressured aquifer and dipping detachments. The basal décollement geometry outlined in Figure 9 is consistent with analyses of thick lithospheres, as inferred from tectonic and gravity studies [*Thurber and Toksoz*, 1978; *McGovern et al*., 2002, 2004b; *Belleguic et al*., 2005].

The observed wrinkle ridges, interacting at depth with the décollement, are therefore the subsequent result of both landslides and gravitational spreading of the edifice. In the eastern province of Olympus Mons, the basal décollement underlying the edifice potentially must act against a regional slope from paleotopography and flexural effects that likely inhibit further gravitational spreading of the edifice [*Byrne et al*., 2013]. Under this scenario, continued gravitational collapse would eventually favor the formation of a new offshoot from the main basal décollement that would occur at depths below the edifice that are not strongly influenced by the current, and/or paleotopographic and flexural effects. The resultant configuration would buttress the eastern slope and begin to retard the failure process in the region, perhaps offering an explanation for why the western flank appears to have failed more catastrophically than in the East.

5.3. Origin of Pore Fluid Overpressures

Excess pore fluid pressure was invoked in previous studies [e.g., *McGovern and Morgan*, 2009] to promote spreading and, in this work, to cause slope failure. Results of this study indicate that both dry, weak sublayers (M1–M5), and sublayers with pore fluid at hydrostatic pressures (M1A–M5A), are insufficient to produce failure for all slopes examined, thus requiring overpressure. In general, high pore fluid pressurization of martian aquifers may be accomplished by several mechanisms. Overpressurization may result from the following: (1) aquifer compaction of sediments due to compression from overburden [*Hubbert and Rubey*, 1959]; (2) dehydration of hydrous minerals at high temperatures generating groundwater of ~4% rock volume [*Bjørlykke*, 1996]; (3) rapid climate change (warm early Mars to cold present-day Mars) resulting in freezing and cryosphere thickening that may have temporarily resulted in pore fluid pressures exceeding lithostatic pressure [*Hanna and Phillips*, 2005]; and (4) tectonic pressurization of aquifers. *Hanna and Phillips* [2006] found that aquifers underlying Athabasca and Mangala Valles, after experiencing single tectonic events, experienced pore fluid pressures that exceeded lithostatic pressure.

The results of *Hanna and Phillips* [2006] are of particular interest. Our values for superlithostatic pressures ($\lambda = 1.6$) in the absence of a dipping substrate, and sublithostatic pressures ($\lambda = 0.8$) with a dipping substrate, may result from ground accelerations derived from events such as deep-seated main décollement slip beneath Olympus Mons, large and/or nearby impacts, or volcanic eruptions. High pore pressures are required to explain faulting geometries along the EOMBS and fall below the upper bound of $\lambda \sim 2$ determined for the regions of Mangala and Athabasca Valles [*Hanna and Phillips*, 2006].

5.4. Implications for Wrinkle Ridges Around Olympus Mons

Wrinkle ridges are one of the most common landforms on Mars [e.g., *Plescia*, 1991, 1993; *Watters and Robinson*, 1997] and can be seen on the Moon [e.g., *Lucchitta*, 1976, 1977; *Sharpton and Head*, 1982], Venus [e.g., *Kreslavsky and Basilevsky*, 1998; *Bilotti and Suppe*, 1999], and Mercury [e.g., *Strom et al*., 1975]. Analogous structures also have been identified on Earth [*Plescia and Golombek*, 1986; *Watters*, 1988]. Although it is generally agreed these are compressional tectonic features formed by folding and thrust faulting, there is no consensus on the number, the geometry, or the maximum depth of faults involved. Moreover, it has been suggested that wrinkle ridges are an expression of either thick-skinned [e.g., *Golombek et al*., 2001; *Montesi and Zuber*, 2003] or thin-skinned deformation [*Watters*, 2004].

The results of our slope and fault analyses along the EOMBS suggest that the wrinkle ridges underlying Olympus Mons are expressions of the compressional toe of a large proto-landslide, at least locally. Consequently, our 2-D models indicate that the depth of crustal penetration does not exceed 5 km. Furthermore, the shape of our calculated failure surface is more consistent with the model of a single listric fault as shown by *Watters* [2004]. Our calculations therefore suggest that these wrinkle ridges are expressions of shallow, thin-skinned deformation from a nascent landslide.

5.5. Implications for Origin of Aureole Lobes

The EOMBS is a unique portion of the Olympus Mons edifice. It is the only area to date in which two slope-parallel fault systems (extensional toward the top of the basal scarp and contractional at its base) have been discovered. It is this discovery, with its unique fault geometry, that allows for a slope stability study to be conducted and constrained by observations.

Our limit equilibrium calculations for the majority of transects along the EOMBS show that the slope is likely conditionally to critically stable and that the observed faults are a direct consequence of a proto-landslide. The volume of material bounded by the inferred slip surface ranges from a lower bound of approximately 5600 km^3 for a phyllosilicate-like substrate at nominal pore pressures, to ~6900 km^3 for deeper, overpressured, and sloping substrates. These volumes account for approximately 32–39% of the material estimated for the "East" Olympus Mons aureole lobe (Figure 1b) by *Griswold et al*. [2008]. A decrease in the volume of potential aureole lobes over time may be expected. As Mars ages, not only may eruptions and impacts be expected to decline but also the availability of water in the near subsurface would likely decrease. As the forces that facilitate failure decline, the scale of the failure should also be expected to decrease. Within this framework, it would be expected that the volume of the already failed slope, deposited as the East aureole lobe, would be greater than the estimated volume of material bounded by the incipient failure surface within the EOMBS.

On the basis of our results, the current basal scarp generally shows increasing instability toward the south and increasing stability to the north along the EOMBS, suggesting that the processes-driving failure are more developed along the south, such that this is where any failure would likely initiate. This observation is critical for understanding (A) how an aureole type event may initiate and (B) the implications for the modification of the entire Olympus Mons edifice.

The southern portion of the EOMBS can be shown, within error, to be critically stable, while the northern portions are more resistant to failure. We argue that only one portion of the edifice in failure may be required to initiate a large-scale flank collapse. Once failure along the south initiates, this effect may propagate along the connected failure trace, in effect "unzipping" this portion of the edifice, allowing for total flank collapse. This allows a relatively small portion of the edifice to drive the failure of a much larger region.

The initial geometry of the failure surface has been shown to be controlled by the topography and depth of the detachment layer, both of which are largely a consequence of volcanic spreading. An examination of Olympus Mons (e.g., Figure 1b) reveals both an asymmetric edifice and aureole lobes, with greater extents to the west and northwest. This work implies that the east-southeast portion of the edifice, including the EOMBS, has experienced less volcanic spreading and is the expression of an early stage of flank failure and aureole lobe formation. Asymmetries in sediment distribution and edifice slopes, in addition to possible buttressing effects from the nearby Tharsis Rise, may play a key role in role in regulating the relative expressions of spreading in different sectors of Olympus Mons [*Morgan and McGovern*, 2005; *McGovern and Morgan*, 2005].

The comparable volume of material estimated to be bounded by the failure surface in the current basal scarp and that estimated to compose the East aureole lobe, together with the strong agreement of faulting locations between observations and modeling results with edifice slopes that are conditionally to critically stable, provide strong evidence of a landslide origin for the basal scarp and aureole lobes of Olympus Mons.

6. Conclusions

Through structural mapping of the EOMBS and surrounding areas, and limit equilibrium modeling of flank collapse, we can determine that the slope-parallel normal faults and wrinkle ridges on the eastern flank of Olympus Mons are consistent with the surface expression of a linked failure surface. Our models are able to identify the existence, depth, and probable thickness of a weak substrate, mechanically consistent with phyllosilicate sediments predating and as such, underlying, the edifice. Results suggest that sediment thicknesses of ~1 km are needed, and these sediments, acting as a décollement, allow for volcanic spreading [e.g., *Morgan and McGovern*, 2005; *McGovern and Morgan*, 2009], and landslides to modify the edifice. The landslide failure surfaces appear to intersect, and appropriate a portion of the décollement at between 0 and −5 km depth, for nominal pore fluid and overpressured conditions, respectively. Wrinkle ridges in the EOMBS region are therefore likely to reflect thin-skinned tectonic deformation.

Models that do not include pore fluid in the weak substrate or include a sediment package less than 1 km thick fail to reproduce the observed faulting geometries. This finding indicates that not only must water be present in a confined aquifer at the time of faulting but it likely needs to be at near-lithostatic (for dipping décollements) or superlithostatic (for horizontal décollements) pressures. In the latter case, this overpressurization may perhaps be the result of tectonic pressurization and/or ground acceleration.

Analyses of transects along the EOMBS show the slope is likely conditionally to critically stable. The volumes of material bounded by the identified failure surface are on the order of magnitude of the adjacent aureole lobes, with the potential failure volumes ranging from 5600–6900 km^3, or ~ 32–39% of the estimated volume of the East Olympus Mons aureole lobe [*Griswold et al*., 2008]. The volume of this failure geometry is controlled by the depth to the detachment layer and topography, both of which are largely a consequence of volcanic spreading. We suggest that the EOMBS has experienced less volcanic spreading than the rest of the edifice and that this region is the expression of early stage flank failure and aureole lobe formation. Conditions favoring slip along the landslide failure surface, such as water available in the confined aquifer, existed in the very recent past, and potentially could be driving deformation to the present.

Acknowledgments
This research was supported by NASA MDAP grant NNX09AI42G. We thank Oded Katz for many interesting discussions and constructive suggestions. We would also like to thank both Laurent Montesi and Paul Byrne for their thorough and constructive reviews.

References

Anderson, M. G., and K. S. Richards (1987), *Slope Stability—Geotechnical Engineering and Geomorphology*, Wiley, Chichester.

Basilevsky, A. T., S. C. Werner, G. Neukum, J. W. Head, S. van Gasselt, K. Gwinner, and B. A. Ivanov (2006), Geologically recent tectonic, volcanic and fluvial activity on the eastern flank of the Olympus Mons volcano, Mars, *Geophys. Res. Lett.*, *33*, L13201, doi:10.1029/2006GL026396.

Belleguic, V., P. Lognonné, and M. Wieczorek (2005), Constraints on the Martian lithosphere from gravity and topography data, *J. Geophys. Res.*, *110*, E11005, doi:10.1029/2005JE002437.

Bibring, J. P., et al. (2006), Global Mineralogical and Aqueous Mars History Derived from OMEGA/Mars Express Data, science 312, 400.

Bilotti, E., and J. Suppe (1999), The global distribution of wrinkle ridges on Venus, *Icarus*, *139*, 137–159.

Bjørlykke, K. (1996), Lithological control on fluid flow in sedimentary basins, in *Fluid Flow and Transport in Rocks—Mechanisms and Effect*, edited by B. Jamtveit and B. W. D. Yardley, pp. 15–34, Chapman & Hall, London.

Borgia, A., J. Burr, W. Montero, and L. D. Morales (1990), Fault propagation folds induced by gravitational failure and slumping of the central Costa Rica volcanic range: Implications for large terrestrial and Martian volcanic edifices, *J. Geophys. Res.*, *95*, 14,357–14,382, doi:10.1029/JB095iB09p14357.

Byrne, P. K., E. P. Holohan, M. Kervyn, B. van Wyk de Vries, V. R. Troll, and J. B. Murray (2013), A sagging-spreading continuum of large volcano structure, 752, *Geology*, *41*, 339–342.

Carr, M. H. (1973), Volcanism on Mars, *J. Geophys. Res.*, *78*, 4049–4062, doi:10.1029/JB078i020p04049.

Christensen, P. R., et al. (2004), The Thermal Emission Imaging System (THEMIS) for the Mars 2001 Odyssey Mission, *Space Sci. Rev.*, *110*(1–2), 85–130, doi:10.1023/B:SPAC.0000021008.16305.94.

De Blasio, F. V. (2011), The aureole of Olympus Mons (Mars) as the compound deposit of submarine landslides, *EPSL*, *312*, 126–139.

Denlinger, R. P., and P. Okubo (1995), Structure of the mobile south flank of Kilauea Volcano Hawaii, *J. Geophys. Res.*, *100*, 24,499–24,507, doi:10.1029/95JB01479.

Fairén, G. A., J. M. Dohm, V. C. Baker, M. A. de Pablo, J. Ruiz, F. Justin, C. Ferris, and R. C. Anderson (2003), Episodic flood inundations of the northern plains of Mars, *Icarus*, *165*, 53–67.

Fellenius, W. O. (1926), *Mechanics of Soils*, Statika Gruntov, Gosstrollzdat.

Francis, P. W., and G. Wadge (1983), The Olympus Mons aureole: Formation by gravitational spreading, *J. Geophys. Res.*, *88*, 8333–8344, doi:10.1029/JB088iB10p08333.

Golombek, M. P., F. S. Anderson, and M. T. Zuber (2001), Martian wrinkle ridge topography: Evidence for subsurface faults from MOLA, *J. Geophys. Res.*, *106*, 23,811–23,821, doi:10.1029/2000JE001308.

Goodman, R. E. (1989), *Introduction to Rock Mechanics*, 2nd ed., John Wiley, N. Y.

Griswold, J., M. H. Bulmer, D. Beller, and P. J. McGovern (2008), An examination of Olympus Mons aureoles, *Lunar Planet. Sci., 39*, abstract 2239.

Gwinner, K., F. Scholten, R. Jaumann, T. Roatsch, J. Oberst, and G. Neukum (2007), Global mapping of Mars by systematic derivation of Mars Express HRSC high-resolution digital elevation models and orthoimages, Paper presented at Extraterrestrial Mapping Workshop on Advances in Planetary Mapping 2007, ISPRS Comm. IV, Working Group 9, Houston, Tex.

Hanna, J. C., and R. J. Phillips (2005), Hydrological modeling of the Martian crust with application to the pressurization of aquifers, *J. Geophys. Res.*, *110*, E01004, doi:10.1029/2004JE002330.

Hanna, J. C., and R. J. Phillips (2006), Tectonic pressurization of aquifers in the formation of Mangala and Athabasca Valles, Mars, *J. Geophys. Res. 111*, E03003, doi:10.1029/2005JE002546.

Harris, S. A. (1977), The aureole of Olympus Mons Mars, *J. Geophys. Res.*, *82*, 3099–3107, doi:10.1029/JB082i020p03099.

Hubbert, M. K., and W. W. Rubey (1959), Role of fluid pressure in mechanics of overthrust faulting: 1. Mechanics of fluid-filled porous solids and its application to overthrust faulting, *Geol. Soc. Am. Bull.*, *70*, 115–166, doi:10.1130/0016-7606(1959)70[115:ROFPIM]2.0.CO;2.

Janbu, N. (1954), Application of composite slip surface for stability analysis, in *Proceedings of the European Conference of Earth Slopes*, vol. 3, pp. 43–49, Stockholm.

Kelley, C. T. (1995), *Iterative Methods for Linear and Nonlinear Equations*, SIAM, Philadelphia.

Kreslavsky, M. A., and A. T. Basilevsky (1998), Morphometry of wrinkle ridges on Venus: Comparison with other planets, *J. Geophys. Res.*, *103*, 11,103–11,111, doi:10.1029/98JE00360.

Lodders, K. (1998), A survey of shergottite, nakhlite and chassigny meteorites whole-rock compositions, *Meteorit. Planet. Sci.*, *33*, A183–A190, doi:10.1111/j.1945-5100.1998.tb01331.x.

Lopes, R. M. C., J. E. Guest, and C. J. Wilson (1980), Origin of the Olympus Mons scarp and aureole, *Moon Planets*, *22*, 221–234.

Lopes, R. M. C., J. E. Guest, K. Hiller, and G. Neukum (1982), Further evidence for a mass movement origin for the Olympus Mons aureole, *J. Geophys. Res.*, *87*, 9917–9928, doi:10.1029/JB087iB12p09917.

Lucchitta, B. K. (1976), Mare ridges and related highland scarps results of vertical tectonism?, in *Proc. Lunar Sci. Conf. 7th*, pp. 2761–2782.

Lucchitta, B. K. (1977), Topography, structure, and mare ridges in southern Mare Imbrium and northern Oceanus Procellarum, in *Proc. Lunar Sci. Conf. 8th*, pp. 2691–2703.

Malin, M. C., et al. (2007), Context Camera Investigation on board the Mars Reconnaissance Orbiter, *J. Geophys. Res.*, *112*, E05S04, doi:10.1029/2006JE002808.

McGovern, P. J., and S. C. Solomon (1993), State of stress, faulting, and eruption characteristics of large volcanoes on Mars, *J. Geophys. Res.*, *98*, 23,553–23,579.

McGovern, P. J., and J. K. Morgan (2005), Spreading of the Olympus Mons volcanic edifice, Mars., *Lunar Planet. Sci., 36*, abstract 2258.

McGovern, P. J., and J. K. Morgan (2009), Volcanic spreading and lateral variations in the structure of Olympus Mons, Mars, *Geology*, *37*, 139–142.

McGovern, P. J., S. C. Solomon, D. E. Smith, M. T. Zuber, M. Simons, M. A. Wieczorek, R. J. Phillips, G. A. Neumann, O. Aharonson, and J. W. Head (2002), Localized gravity/topography admittance and correlation spectra on Mars: Implications for regional and global evolution, *J. Geophys. Res.*, *107*(E12), 5136, doi:10.1029/2002JE001854.

McGovern, P. J., J. R. Smith, J. K. Morgan, and M. H. Bulmer (2004a), The Olympus Mons aureole deposits: New evidence for a flank-failure origin, *J. Geophys. Res.*, *109*, E08008, doi:10.1029/2004JE002258.

McGovern, P. J., S. C. Solomon, D. E. Smith, M. T. Zuber, M. Simons, M. A. Wieczorek, R. J. Phillips, G. A. Neumann, O. Aharonson, and J. W. Head (2004b), Correction to "Localized gravity/topography admittance and correlation spectra on Mars: Implications for regional and global evolution," *J. Geophys. Res.*, *109*, E07007, doi:10.1029/2004JE002286.

Montesi, L. G. J., and M. T. Zuber (2003), Clues to the lithospheric structure of Mars from wrinkle ridge sets and localization instability, *J. Geophys. Res.*, *108*(E6), 5048, doi:10.1029/2002JE001974.

Moore, J. G. (1964), Giant submarine landslides on the Hawaiian Ridge, *U.S. Geol. Surv. Prof. Pap.*, *501D*, D95–D98.

Moore, J. G., D. A. Clague, R. T. Holcomb, P. W. Lipman, W. R. Normark, and M. E. Torresan (1989), Prodigious submarine landslides on the Hawaiian Ridge, *J. Geophys. Res.*, *94*, 17,465–17,484.

Morgan, J. K., and P. J. McGovern (2005), Discrete element simulations of gravitational volcanic deformation: 1. Deformation structures and geometries, *J. Geophys. Res.*, *110*, B05402, doi:10.1029/2004JB003252.

Morgan, J. K., G. F. Moore, D. J. Hills, and S. Leslie (2000), Overthrusting and sediment accretion along Kilauea's mobile south flank, Hawaii: Evidence for volcanic spreading from marine seismic reflection data, *Geology*, *28*, 667–670.

Morris, E. C. (1982), Aureole deposits of the Martian volcano Olympus Mons, *J. Geophys. Res.*, *87*, 1164–1178, doi:10.1029/JB087iB02p01164.

Morris, E. C., and K. L. Tanaka (1994), Geologic maps of the Olympus Mons region of Mars, U.S Geol. Surv. Misc. Invest. Ser. Map, I-2327.

Mouginis-Mark, P. (1993), The influence of oceans on Martian volcanism, LPSC XXIV, 1021.

Nahm, A. L., and R. A. Schultz (2007), Outcrop-scale physical properties of Burns Formation at Meridiani Planum, Mars, *Geophys. Res. Lett.*, *34*, L20203, doi:10.1029/2007GL031005.

Okubo, C. H. (2004), Rock mass strength and slope stability of the Hilina slump, Kīlauea volcano, Hawai'i, *J. Volcanol. Geotherm. Res.*, *138*, 43–76.

Owen, S., P. Segall, J. Freymueller, A. Miklius, R. Denlinger, T. Arnadottir, M. Sako, and R. Bürgmann (1995), Rapid deformation of the south flank of Kilauea Volcano, Hawaii, *Science*, *267*, 1328–1332.

Owen, S., P. Segall, M. Lisowski, A. Miklius, R. Denlinger, and M. Sako (2000), Rapid deformation of Kilauea Volcano: Global positioning system measurements between 1990 and 1996, *J. Geophys. Res.*, *105*, 18,983–18,998, doi:10.1029/2000JB900109.

Plescia, J. B. (1991), Wrinkle ridges in Lunae Planum, Mars: Implications for shortening and strain, *Geophys. Res. Lett.*, *18*, 913–916, doi:10.1029/91GL01070.

Plescia, J. B. (1993), Wrinkle ridges of Arcadia Planitia Mars, *J. Geophys. Res.*, *98*, 15,049–15,059, doi:10.1029/93JE01324.

Plescia, J. B., and M. P. Golombek (1986), Origin of planetary wrinkle ridges based on the study of terrestrial analogs, *Geol. Soc. Am. Bull.*, *97*, 1289–1299.

Sharpton, V. L., and J. W. Head (1982), Stratigraphy and structural evolution of Southern Mare Serenitatis: A reinterpretation based on Apollo Lunar Sounder Experiment data, *J. Geophys. Res.*, *87*, 10,983–10,998, doi:10.1029/JB087iB13p10983.

Smith, D. E., et al. (2001), Mars Orbiter Laser Altimeter: Experiment summary after the first year of global mapping of Mars, *J. Geophys. Res.*, *106*, 23,689–23,722, doi:10.1029/2000JE001364.

Strom, R. G., N. J. Trask, and J. E. Guest (1975), Tectonism and volcanism on Mercury, *J. Geophys. Res.*, *80*, 2478–2507, doi:10.1029/JB080i017p02478.

Tanaka, K. L. (1985), Ice-lubricated gravity spreading of the Olympus Mons aureole deposits, *Icarus*, *62*, 191–206.

Terzaghi, K. (1946), *Theoretical Soil Mechanics*, John Wiley, New York, N. Y.

Thurber, C. H., and M. N. Toksoz (1978), Martian lithospheric thickness from elastic flexure theory, *Geophys. Res. Lett.*, *5*, 977–980, doi:10.1029/GL005i011p00977.

Watters, T. R. (1988), Wrinkle ridge assemblages on the terrestrial planets, *J. Geophys. Res.*, *93*, 10,236–10,254, doi:10.1029/JB093iB09p10236.

Watters, T. R. (2004), Elastic dislocation modeling of wrinkle ridges on Mars, *Icarus*, *171*, 284–294.

Watters, T. R., and M. S. Robinson (1997), Radar and photoclinometric studies of wrinkle ridges on Mars, *J. Geophys. Res.*, *102*, 10,889–10,903, doi:10.1029/97JE00411.

Wilson, L., and P. J. Mouginis-Mark (2003), Phreato-magmatic dike-cryosphere interactions as the origin of small ridges north of Olympus Mons, Mars, *Icarus*, *165*, 242–252.